

# Air pollution satellite-based CO<sub>2</sub> emission inversion: system evaluation, sensitivity analysis, and future research direction

Hui Li<sup>1,2</sup>, Jiaxin Qiu<sup>1,2</sup>, Bo Zheng<sup>1,2,\*</sup>

<sup>1</sup>Shenzhen Key Laboratory of Ecological Remediation and Carbon Sequestration, Institute of Environment and Ecology, Tsinghua Shenzhen International Graduate School, Tsinghua University, Shenzhen 518055, China.

<sup>2</sup>State Environmental Protection Key Laboratory of Sources and Control of Air Pollution Complex, Beijing 100084, China.

Correspondence to: Bo Zheng ([bozheng@sz.tsinghua.edu.cn](mailto:bozheng@sz.tsinghua.edu.cn))

**Abstract.** Simultaneous monitoring of greenhouse gases and air pollutant emissions is crucial for combating global warming and air pollution. We previously established an air pollution satellite-based carbon dioxide (CO<sub>2</sub>) emission inversion system, successfully capturing CO<sub>2</sub> and nitrogen oxides (NO<sub>x</sub>) emission fluctuations amid socioeconomic changes. However, the system's robustness and weaknesses have not yet been fully evaluated. Here, we conduct a comprehensive sensitivity analysis with 31 tests on various factors including prior, model resolution, satellite constraint, and inversion system configuration to assess the vulnerability of emission estimates across temporal, sectoral, and spatial dimensions. The Relative Change (*RC*) between these tests and Base inversion reflects the different configurations' impact on inferred emissions, with one standard deviation ( $1\sigma$ ) of *RC* indicating consistency. Although estimates show increased sensitivity to tested factors at finer scales, the system demonstrates notable robustness, especially for annual national total NO<sub>x</sub> and CO<sub>2</sub> emissions across most tests ( $RC < 4.0\%$ ). Spatiotemporally diverse changes in parameters tend to yield inconsistent impacts ( $1\sigma \geq 4\%$ ) on estimates, and vice versa ( $1\sigma < 4\%$ ). The model resolution, satellite constraint, and NO<sub>x</sub> emission factors emerge as the major influential factors, underscoring their priority for further optimization. Taking daily national total CO<sub>2</sub> emissions as an example, the  $\overline{RC} \pm 1\sigma$  they incur can reach  $-1.2 \pm 6.0\%$ ,  $1.3 \pm 3.9\%$ , and  $10.7 \pm 0.7\%$ , respectively. This study reveals the robustness and areas for improvement in our air pollution satellite-based CO<sub>2</sub> emission inversion system, offering opportunities to enhance the reliability of CO<sub>2</sub> emission monitoring in the future.

## 1 Introduction

The knowledge of emissions, i.e., how much, where, and by what activity pollutants are released into the atmosphere, lays the foundation for understanding the changes in atmospheric compositions and managing emissions toward climate and air quality targets (Meinshausen et al., 2022; Li et al., 2022; Zhang et al., 2019). Anthropogenic emissions are strongly modulated by socioeconomic events (e.g., holidays, economic recession, and recovery), therefore, it is essential to monitor emissions timely to interpret atmospheric species

34 concentrations (Shan et al., 2021; Le Quéré et al., 2021; Guevara et al., 2023). Currently, numerous nations,  
35 particularly those within the Global South (i.e., China), grapple with the dual imperatives of mitigating air  
36 pollution and addressing climate change challenges. To effectively navigate these intertwined challenges in  
37 a harmonized and resource-efficient manner, the development of a system capable of disentangling variations  
38 in emissions and their driving factors for greenhouse gases and air pollutants is indispensable (Ke et al., 2023).

39 Recently, a discernible trend is emerging towards inferring anthropogenic carbon dioxide (CO<sub>2</sub>) emissions  
40 from well-observed and co-emitted air pollutants (i.e., nitrogen dioxide, NO<sub>2</sub>) given their co-emission  
41 characteristics in time and space (Wren et al., 2023; Yang et al., 2023; Liu et al., 2020a; Reuter et al., 2019).  
42 NO<sub>2</sub> forms rapidly after NO is emitted from sources and is also the primary nitrogen oxide detectable by most  
43 satellites (Ye et al., 2016). This makes NO<sub>2</sub> a reliable and widely adopted proxy in nitrogen oxides (NO<sub>x</sub> =  
44 NO<sub>2</sub>+NO) emission inversions. However, the co-emission of NO<sub>x</sub> and CO<sub>2</sub> does not imply synchronized  
45 trends in their emissions, as the CO<sub>2</sub>-to-NO<sub>x</sub> emission ratios and activity trends vary across different sectors  
46 (Li and Zheng, 2024). The introduction of NO<sub>2</sub> in the CO<sub>2</sub> emission estimation presents several distinct  
47 advantages. NO<sub>2</sub> has a short lifetime of several hours, rendering its source-contributing plumes readily  
48 detectable via remote sensing techniques (Goldberg et al., 2019). This short lifespan of NO<sub>2</sub> facilitates mass-  
49 balance approaches for estimating NO<sub>x</sub> emissions, which rely on the assumption of a linear relationship  
50 between NO<sub>2</sub> columns and local NO<sub>x</sub> emissions (Cooper et al., 2017; Mun et al., 2023; Martin et al., 2003).  
51 In contrast, the longevity of CO<sub>2</sub>, spanning hundreds of years, combined with its elevated background  
52 concentration reaching hundreds of parts per million (ppm), obscures the detection of local source-triggered  
53 concentration enhancements (i.e., several ppm) (Nassar et al., 2017; Reuter et al., 2019). Moreover, remote  
54 sensing technologies for NO<sub>2</sub> remain generally more mature, as indicated by the broader coverage and  
55 improved signal-to-noise ratio in column concentration observation (Macdonald et al., 2023; Cooper et al.,  
56 2022). Recent advancements in CO<sub>2</sub> satellite technology are promising, such as the Orbiting Carbon  
57 Observatory-3 (OCO-3), which can generate CO<sub>2</sub> maps with a resolution of up to 1.6 km × 2.2 km and  
58 monitor CO<sub>2</sub> columns at different times throughout the daytime to elucidate diurnal emission patterns (Taylor  
59 et al., 2023), while its spatial coverage may not be sufficient for large-area inversions at high temporal  
60 resolution. The synergistic quantification of CO<sub>2</sub> and NO<sub>x</sub> emissions has gained substantial attention, not to  
61 mention that it could provide valuable guidance for a joint effort to monitor and mitigate air pollutants and  
62 carbon emissions concurrently (Miyazaki and Bowman, 2023).

63 We have developed an air pollution satellite-based CO<sub>2</sub> emission inversion system, which is capable of  
64 concurrently estimating the ten-day moving average of sector-specific anthropogenic NO<sub>x</sub> and CO<sub>2</sub> emissions  
65 by integrating top-down and bottom-up methods. This integrated methodology has proven effective in  
66 capturing emission fluctuations, particularly during the coronavirus disease 2019 (COVID-19) pandemic  
67 (Zheng et al., 2020; Li et al., 2023). While previous sensitivity tests have suggested a certain level of accuracy,  
68 the system has not yet undergone a comprehensive evaluation to thoroughly assess its robustness and  
69 weaknesses, and thereby clearly imply its future developmental trajectory. To bridge this gap, we undertake  
70 an extensive sensitivity analysis with 31 tests using the 2022 anthropogenic NO<sub>x</sub> and CO<sub>2</sub> emission estimation

71 as a case study. This study investigates how emission outcomes respond to a variety of sensitivity assessments  
72 across temporal, sectoral, and spatial dimensions. This study aims to diagnose and rank the uncertainty  
73 sources, providing insights to prioritize improvements of this inversion system in the future.

## 74 **2 Materials and methods**

75 Our air pollution satellite-based CO<sub>2</sub> emission inversion system has been elucidated in our previous studies  
76 (Zheng et al., 2020; Li et al., 2023). In essence, this system integrates top-down and bottom-up data streams  
77 to infer the ten-day moving average of anthropogenic NO<sub>x</sub> and CO<sub>2</sub> emissions by sector in China based on  
78 the mass-balance approach (Cooper et al., 2017). Comprising three key components, the system involves the  
79 bottom-up inference of prior emissions for NO<sub>x</sub> and CO<sub>2</sub> with sectoral profile, the top-down estimation of  
80 total NO<sub>x</sub> emissions constrained by satellite observation, and the integration of both sources to derive  
81 satellite-constrained NO<sub>x</sub> and CO<sub>2</sub> emissions by sector (Fig. S1). Each of these processes could introduce  
82 uncertainties in the final emission estimates. To assess the potential uncertainties, we establish a baseline  
83 (Base) for emissions computed using our conventional settings (Li et al., 2023; Zheng et al., 2020) and further  
84 investigate sensitivity tests to characterize the impacts of the different configurations on final estimates.

### 85 **2.1 Inversion methodology and Base inversion**

86 We use the Base inversion as a case to provide a detailed explanation of this inversion system. In the Base  
87 inversion, we adhered to the same parameters and configurations outlined in previous studies for estimating  
88 the ten-day moving average of anthropogenic NO<sub>x</sub> and CO<sub>2</sub> emissions by sector in 2022 (Table 1) (Li et al.,  
89 2023; Zheng et al., 2020). Succinctly, we first updated sectoral NO<sub>x</sub> and CO<sub>2</sub> emissions from the Multi-  
90 resolution Emission Inventory for China (MEIC) inventory (Zheng et al., 2018) through the bottom-up  
91 process. This involved utilizing indicators including industrial production, thermal power generation, freight  
92 turnover, and population-weighted heating degree days as proxies for changes in industry, power, transport,  
93 and residential activity levels (Details seen in Text S1 and Table S1). Notably, to reconcile the resolution  
94 between the prior emissions and the model, we aggregated the original MEIC emissions from a resolution of  
95 0.25°×0.25° (Fig. S2) to 0.5°×0.625°. Secondly, we inferred the total anthropogenic NO<sub>x</sub> emissions  
96 constrained by TROPospheric Monitoring Instrument (TROPOMI) NO<sub>2</sub> retrievals (v2.4) (Van Geffen et al.,  
97 2022) (Eq. 1). A critical step in this process was establishing a linear relationship between NO<sub>2</sub> tropospheric  
98 vertical column densities (TVCDs) and anthropogenic NO<sub>x</sub> emissions under the mass balance assumption  
99 (Eq. 2) through GEOS-Chem simulation (v12.3.0, <https://geoschem.github.io/>) at a horizontal resolution of  
100 0.5°×0.625°. Our analysis focused on the grids where anthropogenic emissions prevail (Liu et al., 2020b),  
101 characterized by a ten-day moving average of NO<sub>2</sub> TVCDs exceeding 1×10<sup>15</sup> molecules cm<sup>-2</sup>.

$$102 \quad E_{t,i,TROPOMI,y} = (1 + \beta_{t,i} \left( \frac{\Delta\Omega}{\Omega} \right)_{t,i,anth,y}) \times E_{t,i,bottom-up,2019} \quad (1)$$

$$\beta_{t,i} = \frac{\Delta E_{t,i,bottom-up,2019}}{E_{t,i,bottom-up,2019}} \div \frac{\Omega_{t,i,-40\%emi,2019} - \Omega_{t,i,base,2019}}{\Omega_{t,i,base,2019}} \quad (2)$$

$$\left(\frac{\Delta\Omega}{\Omega}\right)_{t,i,anth,y} = \frac{\Omega_{t,i,sate,y}}{\Omega_{t,i,sate,2019}} - \frac{\Omega_{t,i,simu\_fixemis,y}}{\Omega_{t,i,simu,2019}} \quad (3)$$

Where  $t$ ,  $i$ , and  $y$  represent the ten-day window, model grid cell (i.e.,  $0.5^\circ \times 0.625^\circ$ ), and target year 2022, respectively.  $E_{t,i,TROPOMI,y}$  is the anthropogenic total NO<sub>x</sub> emissions constrained by TROPOMI NO<sub>2</sub> TVCDs.  $E_{t,i,bottom-up,2019}$  is the anthropogenic NO<sub>x</sub> emissions in 2019 from the MEIC.  $\beta_{t,i}$  is a unitless factor relating the changes in NO<sub>2</sub> TVCDs to anthropogenic NO<sub>x</sub> emissions (Lamsal et al., 2011).  $\Delta E_{t,i,bottom-up,2019}/E_{t,i,bottom-up,2019}$  represent the implemented 40% reduction in anthropogenic NO<sub>x</sub> emissions over China. The 40% reduction was selected after a series of sensitivity tests, which demonstrated that this perturbation level exerts a limited impact on the  $\beta$  estimates (Zheng et al., 2020).  $\Omega_{t,i,-40\%emi,2019}$  and  $\Omega_{t,i,base,2019}$  are GEOS-Chem simulated NO<sub>2</sub> TVCDs at the TROPOMI overpass time in 2019 with a 40% emission reduction and without any emission reduction, respectively.  $(\Delta\Omega/\Omega)_{t,i,anth,y}$  refers to the relative changes in NO<sub>2</sub> TVCDs due to anthropogenic NO<sub>x</sub> emission changes between 2019 and 2022.  $\Omega_{t,i,sate,y}/\Omega_{t,i,sate,2019}$  indicates the relative differences in TROPOMI NO<sub>2</sub> TVCDs between 2019 and 2022, and  $\Omega_{t,i,simu\_fixemis,y}/\Omega_{t,i,simu,2019}$  represents the relative changes in NO<sub>2</sub> TVCDs caused by inter-annual meteorological variation, which are derived from GEOS-Chem simulations with the fixed 2019 emissions and meteorological field in target year.

Thirdly, we integrated the bottom-up and top-down data flows to yield TROPOMI-constrained sectoral NO<sub>x</sub> emissions. Assuming that each grid's emission variability was primarily driven by its dominant source sectors (contributing over 50%), we utilized the discrepancy between the bottom-up and top-down estimates in grid cells dominated by a particular sector to derive sector-specific scaling factors, which were subsequently applied to correct the bottom-up sectoral NO<sub>x</sub> emissions (Eq. 4). For grids without a sector contributing over 50%, we excluded them from sectoral scaling factor calculations, instead applying scaling factors derived from grids meeting this criterion. The number of these grids accounts for less than 20% of total grids, making their impact negligible. Following this adjustment, we rescaled the corrected bottom-up emissions to ensure alignment with the TROPOMI-constrained total emissions. The overall sectoral correction factors mainly range from 0.5 to 1.5 (Fig. S3).

$$\text{scalefactor}_{t,s,y} = 1 + \frac{\sum_i (E_{t,i,sate,y}^s - E_{t,i,bottom-up,y}^s)}{\sum_i E_{t,i,bottom-up,y}^s} \quad (4)$$

Where  $t$ ,  $s$ ,  $i$ , and  $y$  represent the ten-day window, sector, grid cell (i.e.,  $0.5^\circ \times 0.625^\circ$ ), and year 2022, respectively.  $E_{t,i,sate,y}^s$  and  $E_{t,i,bottom-up,y}^s$  are TROPOMI-constrained and bottom-up estimated NO<sub>x</sub> emissions on grid cell  $i$  with dominated source sector  $s$ , respectively. The  $\text{scalefactor}_{t,s,y}$  is the scaling factor used to correct the bottom-up estimated NO<sub>x</sub> emissions from sectors in time  $t$  in year  $y$ .

Finally, we converted the sectoral NO<sub>x</sub> emissions to corresponding CO<sub>2</sub> emissions with the CO<sub>2</sub>-to-NO<sub>x</sub> emission ratios derived from the bottom-up process (Eq. 5). The CO<sub>2</sub>-to-NO<sub>x</sub> emission ratios in 2022 are updated by reducing NO<sub>x</sub> emission factors (EFs) while keeping CO<sub>2</sub> EFs unchanged based on 2019 MEIC.

136 The default assumption that the reduction rate halves annually is due to the limited potential for further  
 137 reductions. In contrast, the CO<sub>2</sub> EFs are assumed to remain unchanged, as they are primarily determined by  
 138 fuel type and combustion conditions (Cheng et al., 2021) (details seen in Text S2).

$$139 \quad C_{s,t,i,TROPOMI,y} = E_{s,t,i,TROPOMI,y} \times \frac{EF_{CO_2 s,i,bottom-up,2019}}{EF_{NO_x s,i,bottom-up,2019} \times (1 - rNO_{x,s,i,y})} \quad (5)$$

140 Where  $C_{s,t,i,TROPOMI,y}$  and  $E_{s,t,i,TROPOMI,y}$  are CO<sub>2</sub> and NO<sub>x</sub> emissions from sector  $s$ .  $EF_{CO_2 s,i,bottom-up,2019}$  and  
 141  $EF_{NO_x s,i,bottom-up,2019}$  are the sectoral EFs of CO<sub>2</sub> and NO<sub>x</sub> in 2019 derived from the MEIC emission model.  
 142  $rNO_{x,s,i,y}$  is the reduction ratio in NO<sub>x</sub> EFs by sector from 2019 to 2022 derived from the bottom-up estimation.

143 We approximate the annual NO<sub>x</sub> and CO<sub>2</sub> emissions as the sum of the ten-day moving average of NO<sub>x</sub> and  
 144 CO<sub>2</sub> emissions in 2022 with a vacancy in the first and last five days. This approximation, however, does not  
 145 impact our analysis, as our primary objective is to identify potential sources of uncertainty within the system  
 146 and thereby highlight areas for future improvement.

147 **Table 1. Configurations of Base inversion.**

Factors/parameters	Base setting
GEOS-Chem (GC) resolution	GEOS-Chem simulation with the resolution of 0.5°×0.625°
TROPOMI retrievals version	v2.4 of TROPOMI NO <sub>2</sub>
TROPOMI screening schemes	Cloud fraction (CF)<0.4, quality flag (QA)>0.5
Reference year	2019
NO <sub>x</sub> emission factors (EFs)	The reduction ratio of NO <sub>x</sub> EFs halves annually*
Threshold value to identify dominant emission source sectors for each grid	50%
Sectors in bottom-up estimation	8 sectors (power, industry, cement, iron, residential, residential-bio, on-road, and off-road)

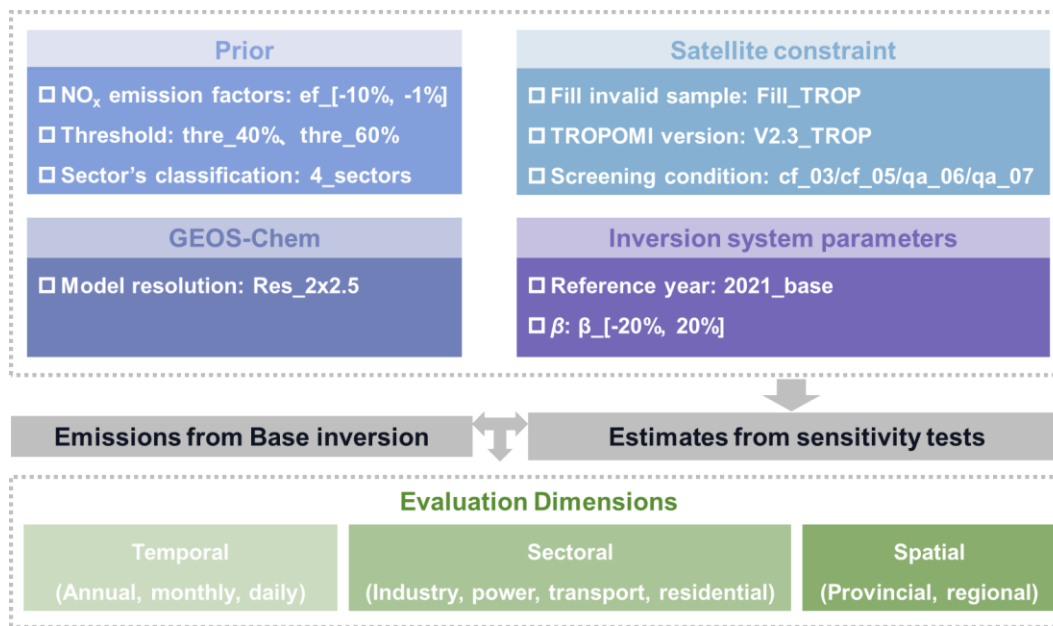
148 \*Each year's reduction rate for NO<sub>x</sub> EFs is set to decrease by half compared to the previous year. For example, if the reduction of NO<sub>x</sub>  
 149 EFs from 2019 to 2020 was 4%, the reduction from 2020 to 2021 would be set at 2%.

## 150 2.2 Sensitivity settings

151 The sensitivity inversion experiments comprise 31 tests designed to provide a comprehensive evaluation of  
 152 the system. To facilitate a clearer discussion of their impacts, we categorized these tests into four classes  
 153 based on their roles within the system: prior information, GEOS-Chem model resolution, satellite  
 154 observational constraints, and inversion system parameters (Fig. 1 and Table 2). Each test is conducted as a  
 155 controlled experiment, where only one parameter is altered while the rest remain the same as their Base  
 156 inversion setting. The rationale behind the settings and their design will be elaborated in the following  
 157 sections.

**Table 2. Settings of 31 sensitivity inversion tests.**

Category	Num	Name	Settings description	Test objectives
GC	1	Res_2×2.5	GEOS-Chem simulation with the resolution of 2°×2.5°	Model resolution
	2	Trop_fill	Complementing TROPOMI NO <sub>2</sub> with machine learning	Sampling coverage
	3	Trop_v2.3	Substituting TROPOMI NO <sub>2</sub> from v2.4 to v2.3	Satellite data version
Satellite constraint	4	Trop_cf03	Changing CF limit from 0.4 to 0.3	Satellite data filtering condition
	5	Trop_cf05	Changing CF limit from 0.4 to 0.5	
	6	Trop_qa06	Changing QA limit from 0.5 to 0.6	
	7	Trop_qa07	Changing QA limit from 0.5 to 0.7	
Inversion system parameters	8	2021_base	Changing the reference year from 2019 to 2021	Reference year
	9	$\beta_{-20\%}$	Scaling $\beta$ down by 20%	$\beta$
	10	$\beta_{-15\%}$	Scaling $\beta$ down by 15%	
	11	$\beta_{-10\%}$	Scaling $\beta$ down by 10%	
	12	$\beta_{-5\%}$	Scaling $\beta$ down by 5%	
	13	$\beta_{-1\%}$	Scaling $\beta$ down by 1%	
	14	$\beta_{1\%}$	Scaling $\beta$ up by 1%	
	15	$\beta_{5\%}$	Scaling $\beta$ up by 5%	
	16	$\beta_{10\%}$	Scaling $\beta$ up by 10%	
	17	$\beta_{15\%}$	Scaling $\beta$ up by 15%	
18	$\beta_{20\%}$	Scaling $\beta$ up by 20%		
Prior	19	ef_-10%	Scaling changes in NO <sub>x</sub> EFs down by 10%	NO <sub>x</sub> EFs
	20	ef_-9%	Scaling changes in NO <sub>x</sub> EFs down by 9%	
	21	ef_-8%	Scaling changes in NO <sub>x</sub> EFs down by 8%	
	22	ef_-7%	Scaling changes in NO <sub>x</sub> EFs down by 7%	
	23	ef_-6%	Scaling changes in NO <sub>x</sub> EFs down by 6%	
	24	ef_-5%	Scaling changes in NO <sub>x</sub> EFs down by 5%	
	25	ef_-4%	Scaling changes in NO <sub>x</sub> EFs down by 4%	
	26	ef_-3%	Scaling changes in NO <sub>x</sub> EFs down by 3%	
	27	ef_-2%	Scaling changes in NO <sub>x</sub> EFs down by 2%	
	28	ef_-1%	Scaling changes in NO <sub>x</sub> EFs down by 1%	
	29	thre_40%	Changing the dominant sector threshold from 50% to 40%	Threshold
	30	thre_60%	Changing the dominant sector threshold from 50% to 60%	
	31	4_sectors	Aggregating the sectors from 8 to 4 in prior estimates	Sector's classification



160

161 **Figure 1. Overview of the sensitivity inversion tests in this study.** Details of the processes and settings are  
 162 presented in Fig. S1 and Table 2.

163 **2.2.1 Modifying prior emission estimates**

164 The prior provides the sectoral profile for subsequent emission attribution. We conducted a comprehensive  
 165 examination of associated parameters when updating the prior from 2019 MEIC (0.5°×0.625°), including  
 166 NO<sub>x</sub> EFs influencing the conversion of NO<sub>x</sub> to CO<sub>2</sub> emissions by sector, threshold value defining the  
 167 dominant sector for each grid, and sector classification. For NO<sub>x</sub> EFs settings, we devised a ten-level gradient  
 168 ranging from -10% to -1% (referred to as ef\_[-10%, -1%]). Regarding the threshold value, we varied it from  
 169 50% to 40% and 60% (referred to as thre\_40% and thre\_60%), respectively. For sector classification, the  
 170 original prior NO<sub>x</sub> and CO<sub>2</sub> emissions were updated based on eight sectors in the bottom-up process: power,  
 171 industry, cement, iron, residential, residential-bio, on-road, and off-road. This detailed sectoral structure  
 172 facilitates relatively detailed bottom-up estimations with specific sectoral activity levels. These eight sectors  
 173 were then aggregated into four categories: power, industry (sum of original industry, cement, and iron),  
 174 residential (sum of original residential and residential-bio), and transport (sum of original on-road and off-  
 175 road) when allocating TROPOMI-constrained total NO<sub>x</sub> emissions into sectors. Here, this sector  
 176 consolidation, specifically implemented before the bottom-up estimation (4\_sectors), was designed to  
 177 evaluate the influence of sector classification on the inversion results.

178 **2.2.2 Employing coarser model resolution**

179 The model resolution of the GEOS-Chem simulation inherently shapes the localized relationship between  
 180 NO<sub>2</sub> TVCDs and NO<sub>x</sub> emissions established in the top-down process. Finer resolution is advantageous for  
 181 establishing localized connections between air pollutant emissions and atmospheric concentrations, and the  
 182 attribution of sectoral emissions. However, excessively fine resolution is not applicable due to the inter-grid

183 transport when employing the mass-balance method (Turner et al., 2012). To explore the impact of resolution  
184 on emission estimates, we performed an inversion experiment with simulations at a coarser resolution of  
185  $2^\circ \times 2.5^\circ$  (Res\_2x2.5).

### 186 **2.2.3 Changing satellite observational constraints**

187 The TROPOMI NO<sub>2</sub> retrievals serve as a constraint in the top-down NO<sub>x</sub> emission estimation. We conducted  
188 experiments on the TROPOMI NO<sub>2</sub> retrievals through three distinct approaches. Firstly, we used Extreme  
189 Gradient Boosting (XGBoost) to fill the invalid satellite retrievals in v2.4 TROPOMI (Trop\_fill) by  
190 establishing relationships between TROPOMI NO<sub>2</sub> TVCDs and meteorological variables, as well as GEOS-  
191 Chem simulated NO<sub>2</sub> TVCDs (modeled\_NO<sub>2</sub> in Eq. 6) (Wei et al., 2022). The meteorological variables were  
192 derived from European Centre for Medium-Range Weather Forecasts (ECMWF) ERA5 dataset (Hersbach et  
193 al., 2020), including boundary layer height (BLH), surface pressure (SP), temperature (TEM), dewpoint  
194 temperature (DT), 10m u-component (WU), 10m v-component of winds (WV), total precipitation (TP),  
195 evaporation (EP), downward uv radiation at the surface (surUV), and mean surface downward uv radiation  
196 flux (downUV). In the XGBoost process, we trained the relationship for daily NO<sub>2</sub> TVCDs throughout the  
197 year grid-by-grid, with 80% of the data used as the training set and 20% as the test set.

$$198 \quad \text{TROPOMI\_NO}_2 \sim f_{\text{XGBoost}}(\text{modeled\_NO}_2, \text{BLH}, \text{SP}, \text{TEM}, \text{DT}, \text{WU}, \text{WV}, \text{TP}, \text{EP}, \text{surUV}, \text{downUV}) \quad (6)$$

199 The comparison of NO<sub>2</sub> TVCDs before and after data filling revealed minimal impact from the original  
200 missing data (Fig. S4). This is attributed to our system's utilization of a ten-day moving average of NO<sub>2</sub>  
201 TVCDs, which effectively mitigates the influence of missing data at the grid scale.

202 Secondly, we evaluated the impact of different versions of TROPOMI NO<sub>2</sub> retrievals by substituting the v2.4  
203 TROPOMI data with the older v2.3 TROPOMI NO<sub>2</sub> columns (Trop\_v2.3). Updates in TROPOMI data  
204 products generally help address the low bias of NO<sub>2</sub> concentrations, particularly in heavily polluted regions  
205 (Lange et al., 2023; Van Geffen et al., 2022). Thirdly, we adjusted the satellite data screening protocols to  
206 investigate the uncertainties associated with satellite observations on emission estimates, which involved  
207 varying the cloud fraction (CF) limit to 0.3 (Trop\_cf03) or 0.5 (Trop\_cf05) and modifying the quality flag  
208 (QA) limit to 0.6 (Trop\_qa06) or 0.7 (Trop\_qa07), respectively. CF and QA serve as crucial parameters in  
209 screening applicable NO<sub>2</sub> TVCDs, representing primary sources of uncertainty in satellite observations (Van  
210 Geffen et al., 2022; Lange et al., 2023).

### 211 **2.2.4 Tests on inversion system parameters**

212 In previous studies, the reference year for updating emissions for target years was 2019. Here, we modified  
213 the reference year to 2021 (2021\_base) to assess its impact. The parameter  $\beta$  represents the localized  
214 relationship between changes in NO<sub>2</sub> TVCDs and changes in anthropogenic NO<sub>x</sub> emissions (Eq. 2),  
215 determining the transition from observed changes in NO<sub>2</sub> TVCDs to changes in anthropogenic NO<sub>x</sub> emissions



216 in the top-down process. To explore potential nonlinear responses in the estimated results to this parameter,  
 217 we devised a ten-level gradient for  $\beta$ , ranging from -20% to 20% (refer to as  $\beta_{[-20\%, 20\%]}$ ).

### 218 2.3 Evaluation of different configurations' impact

219 The sensitivity analysis of the NO<sub>x</sub> and CO<sub>2</sub> emissions estimated by our inversion system has illuminated  
 220 potential sources of uncertainty and the magnitude of their impacts. To quantify the influence of sensitivity  
 221 tests on emission estimates, we calculated the Relative Change ( $RC$ ) between emissions estimated under  
 222 different tests and the Base inversion, and one standard deviation ( $1\sigma$ ) of  $RC$  to evaluate the consistency of  
 223 their impact across temporal, sectoral, and spatial scales (details seen in Table 3). It is noteworthy that on the  
 224 annual national total emission scale (maximization of all three dimensions), the value of  $1\sigma$  equals 0.0%.

225 **Table 3. Calculation of  $RC$  and  $1\sigma$  across different dimensions.**

Dimension	Equations	Parameters
Temporal	$RC_t = \frac{E_{t,sensi} - E_{t,base}}{E_{t,base}}$ $\sigma_t = \sqrt{\frac{\sum_t^n (RC_t - \overline{RC_t})^2}{n}}$	<ul style="list-style-type: none"> <li>• <math>t</math> represents timescale, denoting year, month, or ten-day window.</li> <li>• <math>E_{t,sensi}</math> and <math>E_{t,base}</math> denote the national total emissions under a specific sensitivity test and Base on corresponding temporal scale <math>t</math>.</li> <li>• <math>RC_t</math> and <math>\sigma_t</math> indicate the <math>RC</math> and its <math>1\sigma</math> of national total emissions across temporal scales. The <math>\sigma_t</math> equals 0.0% when <math>t</math> is the yearly scale.</li> </ul>
Sectoral	$RC_{t,s} = \frac{E_{t,s,sensi} - E_{t,s,base}}{E_{t,s,base}}$ $\sigma_s = \sqrt{\frac{\sum_t^n (RC_s - \overline{RC_s})^2}{n}} \quad (\text{Daily})$	<ul style="list-style-type: none"> <li>• <math>s</math> represents sector source.</li> <li>• <math>E_{t,s,sensi}</math> and <math>E_{t,s,base}</math> refer to national sectoral emissions under sensitivity test and Base on temporal scale <math>t</math> (annual and daily).</li> <li>• <math>RC_{t,s}</math> indicates the <math>RC</math> of national sectoral emissions on a temporal scale <math>t</math>.</li> <li>• <math>\sigma_s</math> indicates <math>1\sigma</math> of <math>RC</math> of national sectoral emissions on a daily scale.</li> </ul>
Spatial	$RC_{t,p/r} = \frac{E_{t,p/r,sensi} - E_{t,p/r,base}}{E_{t,p/r,base}}$ $\sigma_p = \sqrt{\frac{\sum_p^m (RC_p - \overline{RC_p})^2}{m}} \quad (\text{Annual})$ $\sigma_r = \sqrt{\frac{\sum_t^n (RC_r - \overline{RC_r})^2}{n}} \quad (\text{Daily})$	<ul style="list-style-type: none"> <li>• <math>p</math> and <math>r</math> represent province and region (i.e., provincial clusters), respectively.</li> <li>• <math>E_{t,p/r,sensi}</math> and <math>E_{t,p/r,base}</math> refer to provincial/regional total emissions under sensitivity test and Base on temporal scale <math>t</math> (annual and daily).</li> <li>• <math>RC_{t,p/r}</math> indicates the <math>RC</math> of provincial/regional total emissions on a temporal scale <math>t</math>.</li> <li>• <math>\sigma_p</math> indicates <math>1\sigma</math> of <math>RC</math> of annual total emissions on the provincial scale.</li> <li>• <math>\sigma_r</math> indicates <math>1\sigma</math> of <math>RC</math> of regional total emissions on a daily scale.</li> </ul>

226

227 In this context, a condition where  $1\sigma$  is below 4.0% is deemed as a consistent impact on emission outcomes  
 228 within certain dimensions (the determination of 4.0% seen in Fig. S5). Conversely, when  $1\sigma$  exceeds or equals  
 229 4.0%, it is indicative of an inconsistent impact. For instance, a daily scale  $\sigma_t$  value of 6.2% in the Res\_2×2.5  
 230 test (Fig. S6) suggests that the model resolution exerts a temporally inconsistent influence on daily emission  
 231 estimates, whereas a daily scale  $\sigma_t = 0.0\%$  under ef\_-10% indicates temporal consistency in its influence.

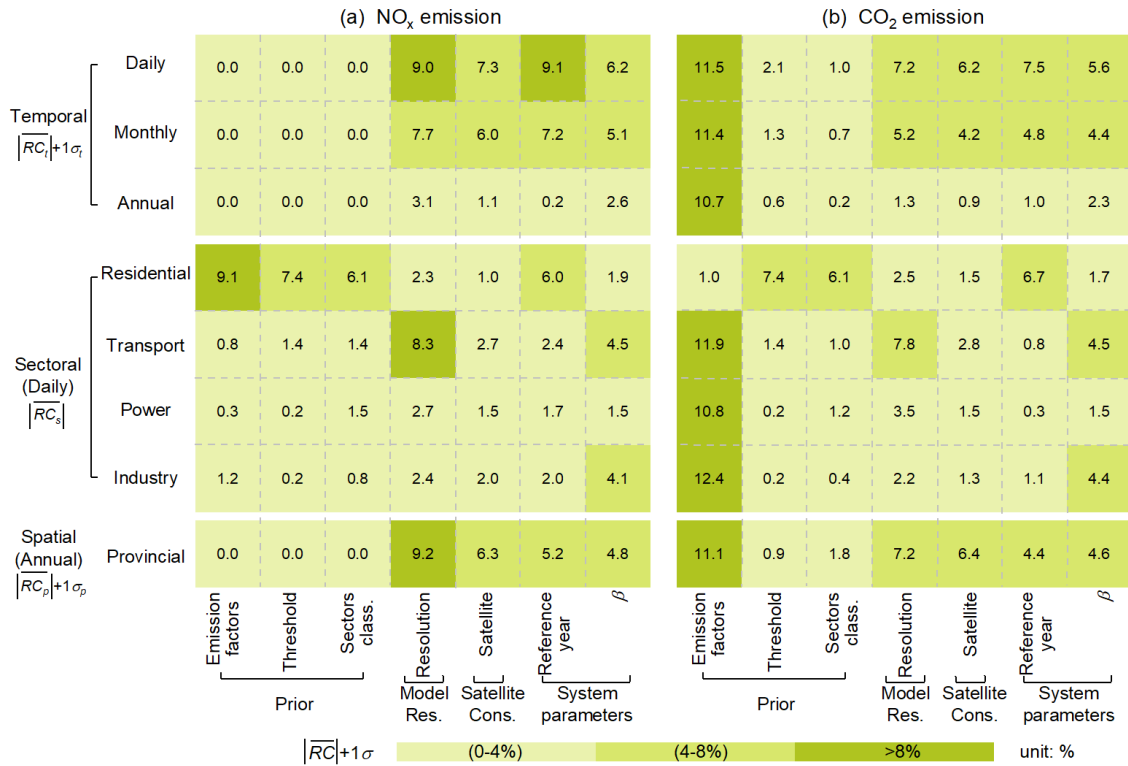
232 These principles extend to other dimensions (i.e., sectoral and spatial). Factors whose sensitivity tests yield  
233 large and inconsistent  $RC$  across finer time, sector, or region scales tend to introduce high uncertainty and  
234 become a priority for future optimization. Conversely, small and consistent  $RC$  suggests sources with low  
235 uncertainty and a higher level of robustness in the system to those particular factors.

### 236 3 Results

#### 237 3.1 Overview of the emission responses to sensitivity tests

238 For a comprehensive understanding of emission sensitivity across various dimensions, we compute the sum  
239 of absolute average  $RC$  and  $1\sigma$  (i.e.,  $|\overline{RC}|+1\sigma$ ) to delineate potential most likely uncertainties associated with  
240 tested factors across spatial, temporal, and sectoral scales (Fig. 2). The impact of these tests on emissions are  
241 comparable between  $\text{NO}_x$  and  $\text{CO}_2$ , except for the  $\text{NO}_x$  EFs tests (first column in Fig. 2), which distinctly  
242 influence  $\text{NO}_x$  and  $\text{CO}_2$  emissions.  $\text{CO}_2$  emissions display high sensitivity to  $\text{NO}_x$  EFs across all dimensions  
243 compared to  $\text{NO}_x$  emissions, except in the residential sector where  $\text{NO}_x$  emissions are more responsive while  
244  $\text{CO}_2$  emissions are not. For instance, ef<sub>-10%</sub> (maximum reduction in  $\text{NO}_x$  EFs tests) incurs a  $|\overline{RC}|+1\sigma$  of  
245 10.7% in annual national  $\text{CO}_2$  emissions, with no corresponding impact on  $\text{NO}_x$  emissions. The relationship  
246 between annual national  $\text{CO}_2$  emissions and  $\text{NO}_x$  EFs exhibits linearity (Fig. S7), remaining within a 4.0%  
247 range if  $\text{NO}_x$  EFs reductions are kept below 4.0% (i.e., ef<sub>[-4%, -1%]</sub>). In contrast, daily residential emissions  
248 show a  $|\overline{RC}|$  of only 1.0% in  $\text{CO}_2$  but up to 9.1% in  $\text{NO}_x$  emissions under the ef<sub>-10%</sub> test.

249 The remaining sensitivity tests, excluding the  $\text{NO}_x$  EFs, demonstrate comparable influences on both  $\text{NO}_x$  and  
250  $\text{CO}_2$  emissions. Among all dimensions examined, the annual national total  $\text{NO}_x$  and  $\text{CO}_2$  emissions emerge  
251 as robust results, with a  $|\overline{RC}|+1\sigma$  of no more than 4.0% across tests. At a finer temporal scale (i.e., daily  
252 basis), the impacts of model resolution, reference year, and satellite constraint on estimated emissions are  
253 amplified, with their  $|\overline{RC}|+1\sigma$  tripling compared to the annual scale. This amplification primarily arises from  
254 the increased  $1\sigma$  on the daily scale (Fig. S6), indicating the substantial impact of these factors on daily  
255 emission estimates. At a finer spatial scale, provincial emissions are vulnerable to changes in model  
256 resolution, reference year, and satellite constraint due to their impacts' inconsistency in space (Fig. S6).  
257 Concerning sectoral emissions, industry and power sector emissions exhibit robustness, whereas transport  
258 and residential emissions present vulnerabilities to model resolution and dominant sector threshold value,  
259 respectively. In the following sections, we elaborate on the impacts of all sensitivity tests on  $\text{NO}_x$  and  $\text{CO}_2$   
260 emissions from temporal, sectoral, and spatial perspectives. To clarify the  $RC$  across different dimensions,  
261 we adopt  $RC_t$ ,  $RC_s$ , and  $RC_{p/r}$  to signify  $RC$  in temporal, sectoral, and spatial contexts, respectively.



262

263 **Figure 2. An overview of sensitivity inversion tests' impacts on (a) NO<sub>x</sub> and (b) CO<sub>2</sub> emissions.** The  
 264 color blocks in this figure represent the sum of absolute average  $RC$  and  $1\sigma$  (i.e.,  $|\overline{RC}|+1\sigma$ ), which reflect  
 265 the extent of the corresponding tests' impact. The numbers within each grid represent the maximum value of  
 266  $|\overline{RC}|+1\sigma$  under tests on corresponding factors. For example, the  $|\overline{RC}|+1\sigma$  noted in the Emission factors  
 267 column refers to ef\_-10%. It is noteworthy that the sectoral dimensions in this figure display their absolute  
 268 average  $RC$  on the daily scale, with their corresponding  $1\sigma$  shown separately in Fig. S6.

### 269 3.2 Emission sensitivity at different temporal scales

270 To exclusively examine emission sensitivities in the temporal dimension, this section focuses on the variation  
 271 of national total emissions in each test. Tests influencing both NO<sub>x</sub> and CO<sub>2</sub> emissions exhibit comparable  
 272 effects, while prior tests exclusively influence CO<sub>2</sub> emissions (Fig. 3). For conciseness, we focus on the  $RC_t$   
 273 in CO<sub>2</sub> emissions in tests here (discussion on NO<sub>x</sub> emissions seen in Text S3). The average  $RC_t$  of national  
 274 total emissions are comparable across temporal scales with differences below 1% (lines in Fig. 3, Figs. S8-  
 275 S9). However, the consistency of  $RC_t$  weakens from yearly to monthly to daily scales (increased  $1\sigma_t$  as shown  
 276 by the shadow in Fig. 3). To better characterize the extent of the tests' impact, the discussion here focuses on  
 277 the  $\overline{RC}_t \pm 1\sigma_t$  on a daily scale, reflecting the magnitude and consistency of the impact concurrently.

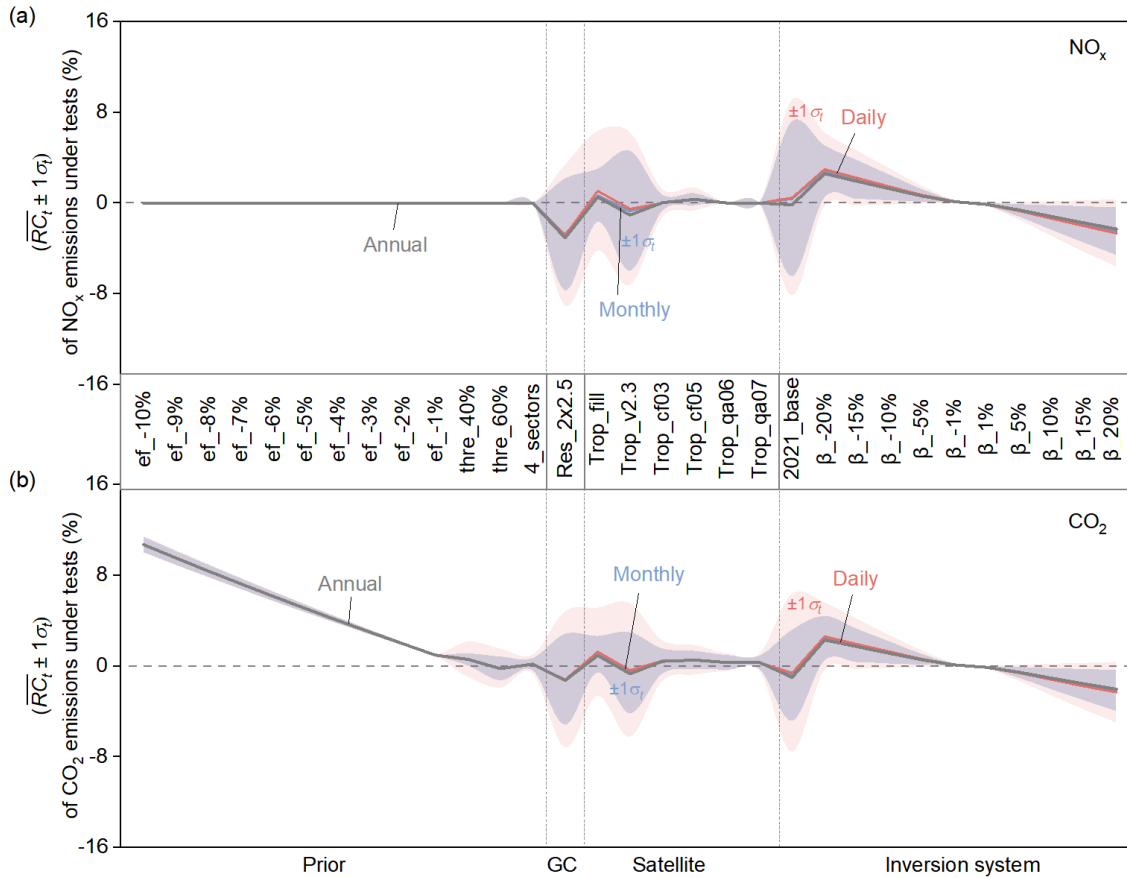
278 At the national total scale, prior tests (ef\_-10%, -1%, thre\_40%/60%, and 4 sectors) influence CO<sub>2</sub>  
 279 emissions consistently over time while leaving NO<sub>x</sub> emissions unaffected (Fig. 3). This occurs because these  
 280 tests only impact sectoral attribution and CO<sub>2</sub>-to-NO<sub>x</sub> emission ratios. Total NO<sub>x</sub> emissions are determined  
 281 in the top-down process before sectoral attribution, thus remaining unchanged (Fig. S1). However, sector-  
 282 specific CO<sub>2</sub> emissions, derived from NO<sub>x</sub> emissions, are influenced due to the varying CO<sub>2</sub>-to-NO<sub>x</sub> emission

283 ratios among sectors (Fig. S10). A reduction in NO<sub>x</sub> EFs increases  $r\text{NO}_x$ , thereby increasing the sectoral CO<sub>2</sub>-  
284 to-NO<sub>x</sub> emission ratios since CO<sub>2</sub> EFs are assumed to be unchanged (Eq. 5). This results in a linear elevation  
285 of CO<sub>2</sub> emissions in tandem with the decreased NO<sub>x</sub> EFs (Fig. S7), with CO<sub>2</sub> emission variations reaching  
286 up to 10.7%±0.7% under  $ef_-$ -10%. Similarly, modifications in threshold values and sector classification alter  
287 the identification of dominant sectors per grid, changing the sectoral attribution. Thre\_40%/60% and  
288 4\_sectors bring about  $\overline{RC}_t \pm 1\sigma_t$  of 0.6%±1.5%, -0.2%±1.7%, and 0.2%±0.8% in CO<sub>2</sub> emissions, respectively,  
289 demonstrating their low influence on emission estimates. Despite differences in the magnitude of prior tests'  
290 impacts ( $\overline{RC}_t$ ), they share a consistency at finer temporal scales, with daily  $1\sigma_t$  below 4.0%.

291 Changes in model resolution (Res\_2×2.5) introduce the largest variation in estimates among all sensitivity  
292 tests, triggering  $\overline{RC}_t \pm 1\sigma_t$  of -1.2%±6.0% in daily CO<sub>2</sub> emissions. Its notable inconsistency of impact on the  
293 finer temporal scale ( $1\sigma_t > 4.0\%$ ) can be traced back to its induced spatiotemporally diverse changes in  $\beta$   
294 (Figs. S11a and S11b). The overall low estimate of  $\beta$  under Res\_2×2.5 results in negative  $RC_t$ , and the uneven  
295 spatial distribution of  $\beta$  explains the large  $1\sigma_t$ .

296 As for the impact of satellite constraint, the systematic changes such as missing value supplementation  
297 (Trop\_fill) or version changes (Trop\_v2.3) have a larger impact with daily CO<sub>2</sub> emission variations of  
298 1.3%±3.9% and -0.4%±5.9%, while alterations in satellite data quality screening conditions  
299 (Trop\_cf/Trop\_qa) exert a relatively minor impact on estimates with  $\overline{RC}_t \pm 1\sigma_t$  less than 0.5%±1.8%. The  
300 spatiotemporal changes in satellite NO<sub>2</sub> retrievals contribute to the inconsistent effects of Trop\_fill and  
301 Trop\_v2.3 on daily emissions. However, the small  $1\sigma_t$  in screening condition tests suggests that the  
302 uncertainty of satellite retrievals has a minor impact on estimates unless there are systematic changes,  
303 possibly because we used the ten-day moving average of satellite observation data to constrain emissions.

304 Among inversion system parameter tests, the alteration of the reference year (2021\_base) exhibits a notable  
305 temporally inconsistent impact, with  $\overline{RC}_t \pm 1\sigma_t$  of -0.6%±6.9% in daily CO<sub>2</sub> emissions. This inconsistency  
306 can be attributed to the spatiotemporally diverse changes in  $\beta$ , similar to the model resolution test (Figs. S11c  
307 and S11d). In contrast, changes in  $\beta$  ( $\beta_{[-20\%, 20\%]}$ ) exert a more notable but consistent impact on estimates,  
308 linearly strengthening as the tested amplitude increases (Fig. S7), with  $\beta_{-20\%}$  triggering variations of  
309 2.6%±3.0% in CO<sub>2</sub> emissions. The spatiotemporally uniform changes in  $\beta$  act linearly on the inversion  
310 estimate of NO<sub>x</sub> emissions (Eq. 1), and then on CO<sub>2</sub> emissions. Therefore, their impact remains consistent on  
311 a daily scale.



312

313 **Figure 3. Comparison of the impacts of various tests on national total (a) NO<sub>x</sub> and (b) CO<sub>2</sub> emissions**  
 314 **at different time scales.** Gray lines correspond to the  $RC_t$  in annual emissions. Blue lines depict the average  
 315  $RC_t$  in monthly emissions, with the blue shadow indicating monthly scale  $1\sigma_t$ . Red lines illustrate the average  
 316  $RC_t$  in daily emissions, accompanied by the red shadow indicating daily scale  $1\sigma_t$ .

### 317 3.3 Emission sensitivity across source sectors

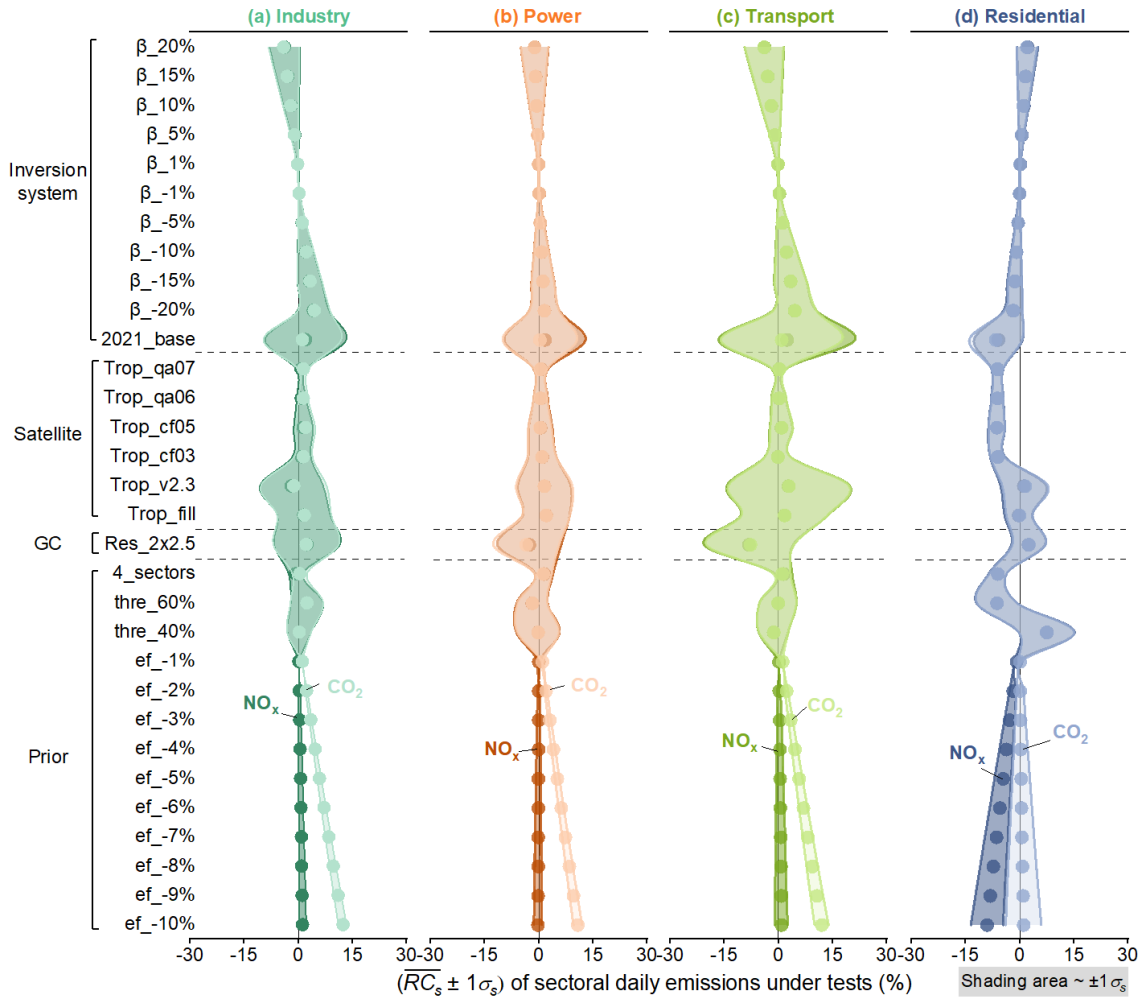
318 Regarding daily national sectoral NO<sub>x</sub> and CO<sub>2</sub> emissions, their responses to different sensitivity tests, in  
 319 terms of both emission magnitude and consistency ( $\overline{RC_s} \pm 1\sigma_s$ ), are largely similar, except for NO<sub>x</sub> EFs tests  
 320 (ef\_<sub>[-10%, -1%]</sub>) (Fig. 4). Therefore, we primarily discuss the impacts of tests on sectoral emissions using  
 321 CO<sub>2</sub> as a representative (refer to Text S4 for discussion on sectoral NO<sub>x</sub> emission), and then delve into  
 322 elucidating the divergent impact of NO<sub>x</sub> EFs on sectoral NO<sub>x</sub> and CO<sub>2</sub> emissions.

323 Irrespective of NO<sub>x</sub> emission factor changes (ef\_<sub>[-10%, -1%]</sub>), industrial and power emissions exhibit greater  
 324 robustness than transport and residential emissions, which are more susceptible to different configurations.  
 325 Specifically, residential emissions demonstrate the highest susceptibility to reference year, showing  
 326  $\overline{RC_s} \pm 1\sigma_s$  of up to  $-6.7\% \pm 7.3\%$  in CO<sub>2</sub> emissions in 2021\_base test, and exclusively display notable  
 327 sensitivity to prior tests (4\_sectors and thre\_40%/60%) compared to other sectors (Fig. 4). In contrast,  
 328 transport emissions are notably influenced by model resolution, with Res\_2x2.5 incurring CO<sub>2</sub> emission  
 329 variations of  $-7.8\% \pm 12.2\%$ . Among all sensitivity tests, the model resolution stands out as the most influential

330 factor on sectoral emissions, because the resolution of grid cells affects the determination of the dominant  
331 source sector.

332 The overall largest sensitivity of residential emissions to sensitivity tests is potentially attributed to its low  
333 proportion to total emissions (Fig. S12). Take  $thre_{40\%/60\%}$  as an example, lowering the threshold from 50%  
334 to 40% results in identifying more grids as residential source dominant. This, in turn, leads to an increase in  
335 residential emission proportions when allocating the total TROPOMI-constrained  $NO_x$  emissions into sectors  
336 and subsequently  $CO_2$  emissions. Conversely, fewer grids are assigned as residential-dominant when the  
337 threshold rises from 50% to 60%, resulting in lower residential emissions (Fig. S13). The next sensitive sector  
338 is transport, particularly vulnerable to model resolution, which may be associated with its characteristics in  
339 spatial distribution. Transport-dominant grids, particularly those with truck emissions, are typically located  
340 close to industry-dominant grids whose  $NO_x$  emissions outweigh those from the transport (Zheng et al., 2020).  
341 The use of a coarser horizontal resolution could result in a diminished attribution of emissions to transport  
342 (Fig. S14).

343 The reduction in  $NO_x$  EFs ( $ef_{[-10\%, -1\%]}$ ) is the only test impacting sectoral  $NO_x$  and  $CO_2$  emissions  
344 differently. For  $NO_x$  emissions, the residential sector shows the strongest sensitivity with  $\overline{RC_s} \pm 1\sigma_s$  of up to  
345  $-9.1\% \pm 4.5\%$  under  $ef_{-10\%}$ . However, its influence on  $CO_2$  emissions is most pronounced in all sectors  
346 except residential, with variations of  $12.4\% \pm 1.1\%$  in  $CO_2$  emissions from industry,  $11.9\% \pm 1.9\%$  from  
347 transport,  $10.8\% \pm 1.2\%$  from power, but only  $1.0\% \pm 4.9\%$  from residential sectors under  $ef_{-10\%}$ . The  
348 reduction in  $NO_x$  EFs shifts the dominant sector attribution, substantially lowering  $NO_x$  emissions from the  
349 residential sector due to its vulnerability to these changes, similar to the impact seen with the  $thre_{60\%}$ . The  
350 other sectoral (industry, transport, and power)  $CO_2$  emissions present stronger sensitivity to  $NO_x$  EFs tests,  
351 linearly correlated with the extent of EFs changes. The decline in sectoral  $NO_x$  EFs linearly reduces  $rNO_x$   
352 (Eq. 5), raising the corresponding  $CO_2$  emissions by increasing sectoral  $CO_2$ -to- $NO_x$  emission ratios.



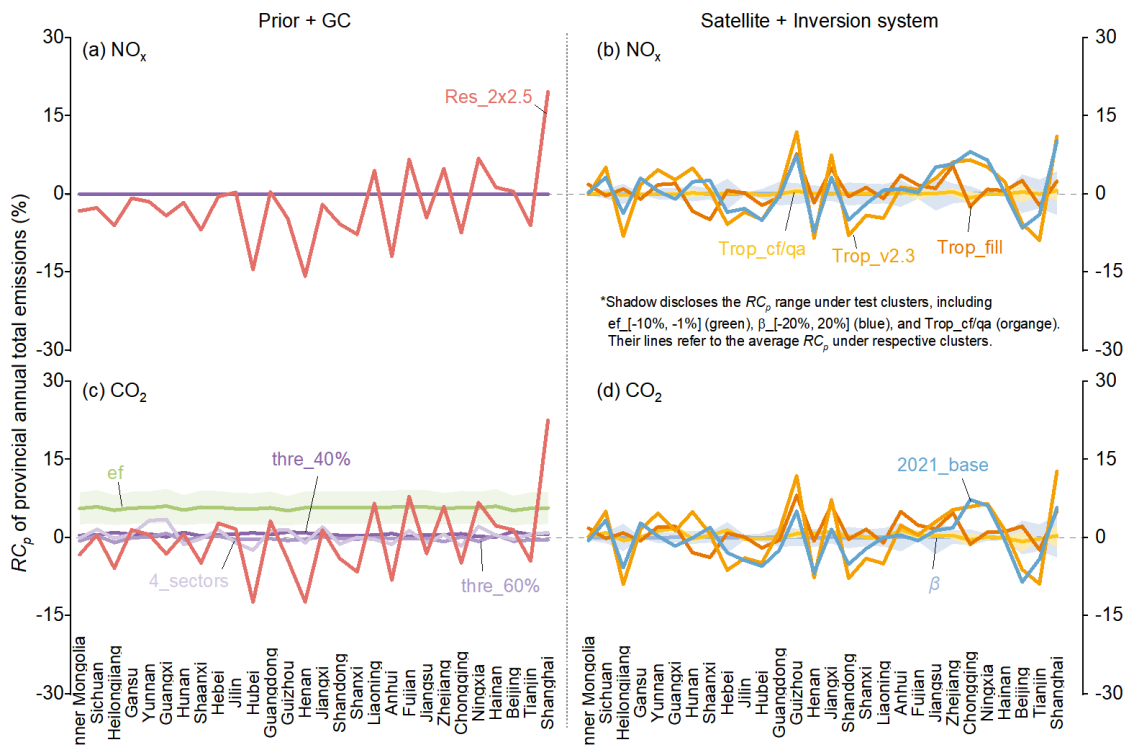
353

354 **Figure 4. Response of sectoral national NO<sub>x</sub> and CO<sub>2</sub> emissions to different sensitivity tests on a daily**  
 355 **scale.** From left to right, the panels correspond to the (a) industry, (b) power, (c) transport, and (d) residential  
 356 source sectors, as the label notes. The dots inside each figure are the average  $RC_s$  of daily NO<sub>x</sub> (deep color)  
 357 and CO<sub>2</sub> (light color) emissions incurred by corresponding tests. The shading area indicates the  $1\sigma_s$  of  
 358 daily sectoral emissions in different tests.

359 **3.4 Emission sensitivity at subnational scales**

360 Refining spatial coverage from national to subnational level (i.e., province) reveals that factors causing  
 361 inconsistent impacts over finer time scales also tend to induce inconsistent impacts on more granular spatial  
 362 regions (Fig. 5). On the annual total scales, the  $RC_p$  of NO<sub>x</sub> and CO<sub>2</sub> emissions at the provincial scale closely  
 363 resemble each other under most sensitivity tests, except for prior tests that only influence CO<sub>2</sub> emissions (Fig.  
 364 S15). When comparing across provinces, the sensitivity of emissions to tests correlates with the size of the  
 365 provincial area, with smaller regions exhibiting greater susceptibility. Shanghai, the smallest provincial-level  
 366 administrative unit in China in terms of area, experiences the largest  $RC_p$  throughout China in nearly all tests.  
 367 Conversely, Inner Mongolia, one of China's top three largest provinces, undergoes the minimum  $RC_p$  in all  
 368 tests. Under Res\_2×2.5, the  $RC_p$  of annual total NO<sub>x</sub> and CO<sub>2</sub> emissions in Shanghai are 19.6% and 22.6%,  
 369 respectively, while in Inner Mongolia, they are -3.2% and -3.3%. Employing a resolution of 2°×2.5° in

370 Shanghai is impractical in real-world applications, as it would result in fewer than two grids covering the  
 371 area. Henan also encounters substantial  $RC_p$  under Res\_2x2.5, reaching as high as -15.8% and -12.4% in  
 372 annual total  $NO_x$  and  $CO_2$  emissions. This could be attributed to its proximity to Shandong, a province with  
 373 approximately twice the emissions of Henan, making Henan particularly sensitive to the changes in model  
 374 resolution due to the overlapping grid cells. It is noteworthy that Guizhou exhibits the highest sensitivity to  
 375 satellite constraint, with  $RC_p$  reaching up to 11.9% and 11.8% in annual total  $NO_x$  and  $CO_2$  emissions under  
 376 Trop\_v2.3. This sensitivity is attributed to the high cloudiness of the Yunnan-Guizhou Plateau, causing  
 377 satellite observations to be highly uncertain over Guizhou (Wang et al., 2023; Li et al., 2021; Cai et al., 2022).



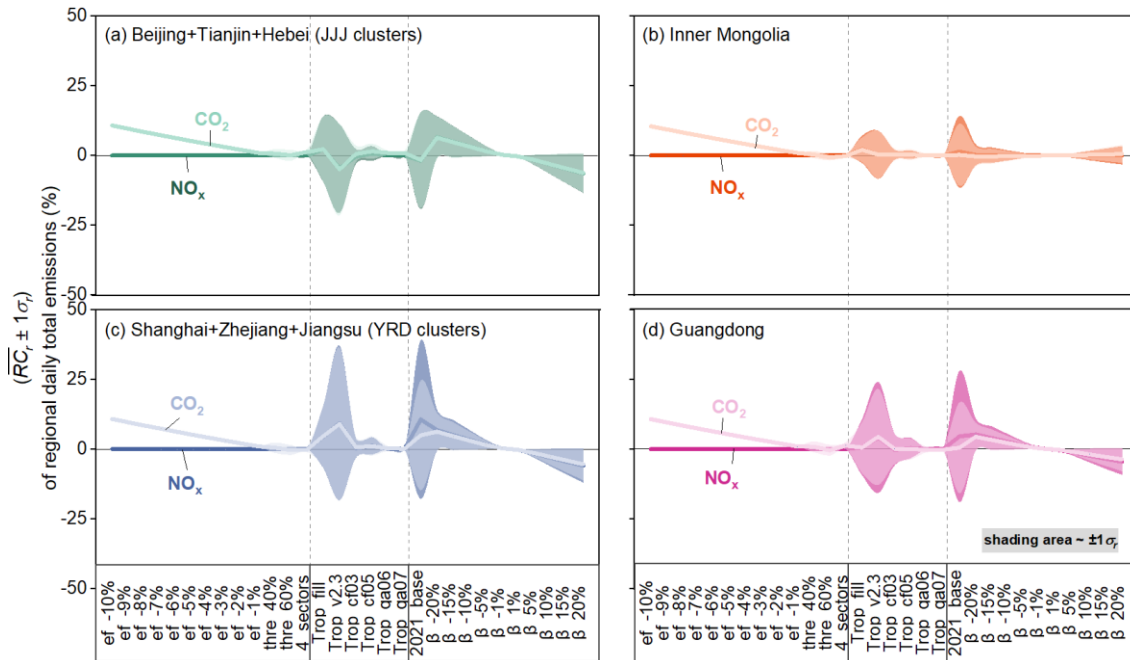
378

379 **Figure 5. Response of provincial annual total  $NO_x$  and  $CO_2$  emissions to different tests.** (a) and (b) show  
 380  $RC_p$  of  $NO_x$  emissions incurred by tests. (c) and (d) are plotted for  $CO_2$  emission as (a) and (b). Lines refer  
 381 to the  $RC_p$  caused by the corresponding test or the averaged  $RC_p$  caused by corresponding test clusters (ef\_[-  
 382 10%, -1%] and  $\beta$  [-20%, 20%]), and the shadow refers to the  $RC_p$  range in test clusters. Only provinces with  
 383 enough TROPOMI observations are shown here (i.e., grids with  $NO_2$  TVCDs larger than  $1 \times 10^{15}$   
 384 molecules/cm<sup>2</sup> cover more than 90% of anthropogenic  $NO_x$  emissions within provinces). The provinces are  
 385 arranged by area.

386 To further investigate the daily total emission response ( $\overline{RC_r} \pm 1\sigma_r$ ) to tests at the regional scale, we select  
 387 and analyze Jing-Jin-Ji clusters (JJJ, including Beijing, Tianjin, and Hebei), Inner Mongolia, Yangtze River  
 388 Delta clusters (YRD, including Shanghai, Zhejiang, and Jiangsu), and Guangdong (the location of the Pearl  
 389 River Delta). These regions respectively represent an industrialized region with high population density, an  
 390 industrialized region with sparse population density, and two major economic development zones with high  
 391 population density in China (Fig. 6). Geographically, these regions span North China (JJJ and Inner  
 392 Mongolia), East China (YRD), and South China (Guangdong), thereby covering different meteorological and



393 geographic factors. Overall, the  $\overline{RC_r} \pm 1\sigma_r$  of daily regional emissions are similar for NO<sub>x</sub> and CO<sub>2</sub> except for  
 394 ef<sub>[-10%, -1%]</sub>, resembling their daily national emission responses (Fig. 3). The  $\overline{RC_r} \pm 1\sigma_r$  of daily regional  
 395 emissions is especially notable in YRD and Guangdong (southern part of China). This could be attributed to  
 396 the relatively low NO<sub>2</sub> concentration in southern China (Fig. S4), making them particularly sensitive to spatial  
 397 variations in parameters, such as the  $\beta$  in 2021\_base (Fig. S11) and NO<sub>2</sub> TVCDs in Trop\_v2.3 test. Besides,  
 398 the cloud fraction is higher in southern China, introducing larger uncertainties in remote sensing (Liu et al.,  
 399 2019; Latsch et al., 2022). The emission responses to prior and  $\beta$ <sub>[-20%, 20%]</sub> tests are close for these four  
 400 regions, particularly in the prior tests, suggesting that these impacts on emissions are less dependent on  
 401 geographic factors.



402  
 403 **Figure 6. Response of regional total NO<sub>x</sub> and CO<sub>2</sub> emissions to tests on a daily scale.** (a), (b), (c), and (d)  
 404 show the  $\overline{RC_r} \pm 1\sigma_r$  of daily NO<sub>x</sub> (deep color) and CO<sub>2</sub> (light color) emissions in different tests in Jing-Jin-Ji  
 405 clusters (Beijing, Tianjin, and Hebei), Inner Mongolia, Yangtze River Delta clusters (Shanghai, Zhejiang,  
 406 and Jiangsu), and Guangdong. The shading area inside each figure refers to the corresponding 1 $\sigma_r$ . It is worth  
 407 noting that the Res\_2 $\times$ 2.5 test is not shown here since the resolution of 2 $^\circ$  $\times$ 2.5 $^\circ$  proves too coarse for certain  
 408 regions, rendering it unrealistic for real-world applications. The result containing Res\_2 $\times$ 2.5 is present in SI  
 409 as Fig. S16 for reference.

#### 410 4 Discussion

411 This study delineates an approximate spectrum of uncertainties inherent in deriving conclusions of varying  
 412 precision with our air pollution satellite-based CO<sub>2</sub> emission inversion system. When interpreting conclusions  
 413 based on the emission data derived from such an inversion system, it is practical and imperative to aggregate  
 414 emissions across different dimensions to fulfill specific usage requirements. Direct utilization of data with  
 415 all fine-grained resolutions at temporal, sectoral, and spatial dimensions poses challenges. If adhering to a

416 variation tolerance of 5%, the reliability of annual national NO<sub>x</sub> and CO<sub>2</sub> emissions is established in most  
417 cases. Notably, careful attention is needed when selecting model resolution and attributing sectoral emissions.  
418 Expanding the tolerance to 10%, which is still below the conventional bottom-up method's uncertainty range  
419 of 13%-37% (Zhao et al., 2011; Huo et al., 2022), renders annual regional or daily national emissions robust  
420 from an average perspective. Nevertheless, meticulous scrutiny is advised when drawing conclusions based  
421 on daily sectoral or daily regional emissions, especially in specific regions (e.g., Shanghai, Guizhou). The  
422 large uncertainty of daily sectoral emission is typically observed in other emission datasets, such as Carbon  
423 Monitor (up to 40% uncertainty) (Liu et al., 2020c; Huo et al., 2022). Further liberalizing the tolerance to  
424 25%, which is quite uncertain for scientific and policy-making purposes, the majority of conclusions derived  
425 from our estimates stand as reliable. The extensive tolerance range primarily stems from regional emissions,  
426 posing a challenging issue for many emission inversion techniques. For example, the uncertainty in NO<sub>x</sub>  
427 emissions derived from the 2D MISATEAM (chemical transport Model-Independent SATellite-derived  
428 Emission estimation Algorithm for Mixed-sources) method is approximately 20% for large and mid-size US  
429 cities (Liu et al., 2023), and the uncertainty for daily NO<sub>x</sub> and CO<sub>2</sub> emissions based on the superposition  
430 model ranges from 37% to 48% on a city scale (Zhang et al., 2023). Notably, remarkable advancements have  
431 been achieved in estimating subnational CO<sub>2</sub> emissions through CO<sub>2</sub>-observing satellites, such as sectoral  
432 CO<sub>2</sub> assessments with OCO-3 (Roten et al., 2023), and urban emission optimizations utilizing the Orbiting  
433 Carbon Observatory-2 (OCO-2) (Yang et al., 2020; Ye et al., 2020). Yet, reducing uncertainties at subnational  
434 scales remains an ongoing challenge.

435 This study paves the way for the continuous improvement of the current air pollution satellite-based CO<sub>2</sub>  
436 emission inversion system. Firstly, prioritizing a nimble and appropriate horizontal resolution is crucial for  
437 establishing accurate localized relationships between NO<sub>2</sub> TVCDs and NO<sub>x</sub> emissions, contributing to  
438 improved NO<sub>x</sub> and CO<sub>2</sub> emission estimations from temporal, sectoral, and spatial perspectives. Secondly, the  
439 more accurate satellite observation is conducive to reducing the uncertainty in final results, presenting  
440 increasing promise with advancements in remote sensing technology. Besides, the progress in multi-species  
441 synchronous observations through satellite and aircraft platforms offers alternative verification for multi-  
442 species emission inversion, such as the Copernicus Anthropogenic Carbon Dioxide Monitoring constellation  
443 (CO2M) (Sierk et al., 2021). Thirdly, the reliability of sectoral NO<sub>x</sub> EFs changes, which determine CO<sub>2</sub>-to-  
444 NO<sub>x</sub> emission ratios, is essential for the accurate conversion from NO<sub>x</sub> to CO<sub>2</sub> emissions. This underscores  
445 the need to acquire more accurate NO<sub>x</sub> EFs. While obtaining on-site measurements of CO<sub>2</sub>-to-NO<sub>x</sub> emission  
446 ratios is challenging, efforts are underway to enhance its configuration. An iterative modification of NO<sub>x</sub> EFs  
447 within the current system could be incorporated, minimizing the gap between bottom-up updated and  
448 TROPOMI-constrained sectoral NO<sub>x</sub> emissions to below 2%. This approach yields more accurate CO<sub>2</sub>-to-  
449 NO<sub>x</sub> emission ratios and CO<sub>2</sub> emissions (Fig. S17). The optimized CO<sub>2</sub> emission change from 2021 to 2022  
450 is +0.6%, reflecting a more precise representation of the growth in fossil fuel consumption (+1.9%). Fourthly,  
451 utilizing a more refined approach to determine dominant sectors at a grid level can reduce the uncertainty of  
452 small-contributing sectoral emissions, particularly in the residential sector. These enhancements will improve

453 the system's accuracy in estimating emissions across all dimensions, positioning it as a valuable tool for  
454 simultaneous inversion-based monitoring of greenhouse gas and air pollutants emissions, ultimately  
455 supporting a strategic roadmap for the vision of clean air and climate warming mitigation.

456

457 *Code and data availability.* The source code of the GEOS-Chem model is available at  
458 <https://geoschem.github.io/>. The prior NO<sub>x</sub> and CO<sub>2</sub> emissions of 2019 MEIC (v1.4) are available at  
459 [http://meicmodel.org.cn/?page\\_id=541&lang=en](http://meicmodel.org.cn/?page_id=541&lang=en). The v2.4.0 TROPOMI NO<sub>2</sub> column concentrations are  
460 publicly available at [https://www.temis.nl/airpollution/no2col/no2regio\\_tropomi.php](https://www.temis.nl/airpollution/no2col/no2regio_tropomi.php). The activity level data  
461 of China from 2019 to 2022 including the industrial production of cement, iron, thermal electricity, etc., are  
462 available at <https://data.stats.gov.cn/english/easyquery.htm?cn=C01>.

463 *Supplement.* The supplement related to this article is available online.

464 *Author Contributions.* Bo Zheng designed the research and led the analysis. Hui Li performed the simulation,  
465 analyzed the data, and created the graphs. Bo Zheng, Jiabin Qiu, and Hui Li wrote the manuscript.

466 *Competing interests.* The authors declare that they have no conflict of interest.

467 *Acknowledgements.* The authors thank the editor and the anonymous referees for helpful comments that have  
468 improved the paper.

469 *Financial support.* This work was supported by the National Key R&D Program of China (2023YFC3705601)  
470 and National Natural Science Foundation of China (Grant No. 42375096).

471 **References**

- 472 Cai, D., Tao, L., Yang, X.-Q., Sang, X., Fang, J., Sun, X., Wang, W., and Yan, H.: A climate  
473 perspective of the quasi-stationary front in southwestern China: structure, variation and impact,  
474 *Climate Dynamics*, 59, 547-560, [10.1007/s00382-022-06151-1](https://doi.org/10.1007/s00382-022-06151-1), 2022.
- 475 Cheng, J., Tong, D., Liu, Y., Bo, Y., Zheng, B., Geng, G., He, K., and Zhang, Q.: Air quality and  
476 health benefits of China's current and upcoming clean air policies, *Faraday Discussions*, 226,  
477 584-606, <https://doi.org/10.1039/D0FD00090F>, 2021.
- 478 Cooper, M., Martin, R. V., Padmanabhan, A., and Henze, D. K.: Comparing mass balance and  
479 adjoint methods for inverse modeling of nitrogen dioxide columns for global nitrogen oxide  
480 emissions, *Journal of Geophysical Research: Atmospheres*, 122, 4718-4734,  
481 [10.1002/2016JD025985](https://doi.org/10.1002/2016JD025985), 2017.
- 482 Cooper, M. J., Martin, R. V., Hammer, M. S., Levelt, P. F., Veefkind, P., Lamsal, L. N., Krotkov, N.  
483 A., Brook, J. R., and McLinden, C. A.: Global fine-scale changes in ambient NO<sub>2</sub> during COVID-19  
484 lockdowns, *Nature*, 601, 380-387, <https://doi.org/10.1038/s41586-021-04229-0>, 2022.
- 485 Goldberg, D. L., Lu, Z., Oda, T., Lamsal, L. N., Liu, F., Griffin, D., McLinden, C. A., Krotkov, N. A.,  
486 Duncan, B. N., and Streets, D. G.: Exploiting OMI NO<sub>2</sub> satellite observations to infer fossil-fuel  
487 CO<sub>2</sub> emissions from U.S. megacities, *Science of The Total Environment*, 695, 133805,  
488 [10.1016/j.scitotenv.2019.133805](https://doi.org/10.1016/j.scitotenv.2019.133805), 2019.
- 489 Guevara, M., Petetin, H., Jorba, O., Denier van der Gon, H., Kuenen, J., Super, I., Granier, C.,  
490 Doumbia, T., Ciais, P., Liu, Z., Lamboll, R. D., Schindlbacher, S., Matthews, B., and Pérez García-  
491 Pando, C.: Towards near-real-time air pollutant and greenhouse gas emissions: lessons learned  
492 from multiple estimates during the COVID-19 pandemic, *Atmospheric Chemistry and Physics*, 23,  
493 8081-8101, <https://doi.org/10.5194/acp-23-8081-2023>, 2023.
- 494 Hersbach, H., Bell, B., Berrisford, P., Hirahara, S., and Thépaut, J.: The ERA5 global reanalysis,  
495 *Quarterly Journal of the Royal Meteorological Society*, 2020.
- 496 Huo, D., Liu, K., Liu, J., Huang, Y., Sun, T., Sun, Y., Si, C., Liu, J., Huang, X., Qiu, J., Wang, H., Cui, D.,  
497 Zhu, B., Deng, Z., Ke, P., Shan, Y., Boucher, O., Darnet, G., Liang, G., Zhao, J., Chen, L., Zhang, Q.,  
498 Ciais, P., Zhou, W., and Liu, Z.: Near-real-time daily estimates of fossil fuel CO<sub>2</sub> emissions from  
499 major high-emission cities in China, *Sci Data*, 9, 684, [10.1038/s41597-022-01796-3](https://doi.org/10.1038/s41597-022-01796-3), 2022.
- 500 Ke, P., Deng, Z., Zhu, B., Zheng, B., Wang, Y., Boucher, O., Arous, S. B., Zhou, C., Andrew, R. M.,  
501 Dou, X., Sun, T., Song, X., Li, Z., Yan, F., Cui, D., Hu, Y., Huo, D., Chang, J.-P., Engelen, R., Davis, S.  
502 J., Ciais, P., and Liu, Z.: Carbon Monitor Europe near-real-time daily CO<sub>2</sub> emissions for 27 EU  
503 countries and the United Kingdom, *Scientific Data*, 10, 374, [10.1038/s41597-023-02284-y](https://doi.org/10.1038/s41597-023-02284-y), 2023.
- 504 Lamsal, L. N., Martin, R. V., Padmanabhan, A., van Donkelaar, A., Zhang, Q., Sioris, C. E., Chance,  
505 K., Kurosu, T. P., and Newchurch, M. J.: Application of satellite observations for timely updates  
506 to global anthropogenic NO<sub>x</sub> emission inventories, *Geophysical Research Letters*, 38,  
507 <https://doi.org/10.1029/2010gl046476>, 2011.
- 508 Lange, K., Richter, A., Schönhardt, A., Meier, A. C., Bösch, T., Seyler, A., Krause, K., Behrens, L. K.,  
509 Wittrock, F., Merlaud, A., Tack, F., Fayt, C., Friedrich, M. M., Dimitropoulou, E., Van Roozendaal,  
510 M., Kumar, V., Donner, S., Dörner, S., Lauster, B., Razi, M., Borger, C., Uhlmannsiek, K., Wagner,  
511 T., Ruhtz, T., Eskes, H., Bohn, B., Santana Diaz, D., Abuhassan, N., Schüttemeyer, D., and  
512 Burrows, J. P.: Validation of Sentinel-5P TROPOMI tropospheric NO<sub>2</sub> products by comparison  
513 with NO<sub>2</sub> measurements from airborne imaging DOAS, ground-based stationary DOAS, and  
514 mobile car DOAS measurements during the S5P-VAL-DE-Ruhr campaign, *Atmos. Meas. Tech.*, 16,  
515 1357-1389, <https://doi.org/10.5194/amt-16-1357-2023>, 2023.
- 516 Latsch, M., Richter, A., Eskes, H., Sneep, M., Wang, P., Veefkind, P., Lutz, R., Loyola, D., Argyrouli,  
517 A., Valks, P., Wagner, T., Sihler, H., van Roozendaal, M., Theys, N., Yu, H., Siddans, R., and

518 Burrows, J. P.: Intercomparison of Sentinel-5P TROPOMI cloud products for tropospheric trace  
519 gas retrievals, *Atmos. Meas. Tech.*, 15, 6257-6283, 10.5194/amt-15-6257-2022, 2022.

520 Le Quéré, C., Peters, G. P., Friedlingstein, P., Andrew, R. M., Canadell, J. G., Davis, S. J., Jackson,  
521 R. B., and Jones, M. W.: Fossil CO<sub>2</sub> emissions in the post-COVID-19 era, *Nature Climate Change*,  
522 11, 197-199, <https://doi.org/10.1038/s41558-021-01001-0>, 2021.

523 Li, H. and Zheng, B.: Toward monitoring daily anthropogenic CO<sub>2</sub> emissions with air pollution  
524 sensors from space, *One Earth*, 7, 1846-1857, 10.1016/j.oneear.2024.08.019, 2024.

525 Li, H., Zheng, B., Ciais, P., Boersma, K. F., Riess, T. C. V. W., Martin, R. V., Broquet, G., van der A,  
526 R., Li, H., Hong, C., Lei, Y., Kong, Y., Zhang, Q., and He, K.: Satellite reveals a steep decline in  
527 China's CO<sub>2</sub> emissions in early 2022, *Science Advances*, 9, eadg7429,  
528 <https://doi.org/10.1126/sciadv.adg7429>, 2023.

529 Li, J., Sun, Z., Liu, Y., You, Q., Chen, G., and Bao, Q.: Top-of-Atmosphere Radiation Budget and  
530 Cloud Radiative Effects Over the Tibetan Plateau and Adjacent Monsoon Regions From CMIP6  
531 Simulations, *Journal of Geophysical Research: Atmospheres*, 126, e2020JD034345,  
532 10.1029/2020JD034345, 2021.

533 Li, L., Zhang, Y., Zhou, T., Wang, K., Wang, C., Wang, T., Yuan, L., An, K., Zhou, C., and Lu, G.:  
534 Mitigation of China's carbon neutrality to global warming, *Nat Commun*, 13, 5315,  
535 10.1038/s41467-022-33047-9, 2022.

536 Liu, F., Duncan, B. N., Krotkov, N. A., Lamsal, L. N., Beirle, S., Griffin, D., McLinden, C. A.,  
537 Goldberg, D. L., and Lu, Z.: A methodology to constrain carbon dioxide emissions from coal-fired  
538 power plants using satellite observations of co-emitted nitrogen dioxide, *Atmos. Chem. Phys.*,  
539 20, 99-116, <https://doi.org/10.5194/acp-20-99-2020>, 2020a.

540 Liu, F., Beirle, S., Joiner, J., Choi, S., Tao, Z., Knowland, K. E., Smith, S. J., Tong, D. Q., Ma, S.,  
541 Fasnacht, Z. T., and Wagner, T.: High-resolution Mapping of Nitrogen Oxide Emissions in Large  
542 US Cities from TROPOMI Retrievals of Tropospheric Nitrogen Dioxide Columns, *EGU sphere*,  
543 2023, 1-18, 10.5194/egusphere-2023-1842, 2023.

544 Liu, F., Page, A., Strode, S. A., Yoshida, Y., Choi, S., Zheng, B., Lamsal, L. N., Li, C., Krotkov, N. A.,  
545 Eskes, H., van der A, R., Veeckind, P., Levelt, P. F., Hauser, O. P., and Joiner, J.: Abrupt decline in  
546 tropospheric nitrogen dioxide over China after the outbreak of COVID-19, *Science Advances*, 6,  
547 eabc2992, <https://doi.org/10.1126/sciadv.abc2992>, 2020b.

548 Liu, Y., Tang, Y., Hua, S., Luo, R., and Zhu, Q.: Features of the Cloud Base Height and Determining  
549 the Threshold of Relative Humidity over Southeast China, *Remote Sensing*, 11, 2900, 2019.

550 Liu, Z., Ciais, P., Deng, Z., Lei, R., Davis, S. J., Feng, S., Zheng, B., Cui, D., Dou, X., Zhu, B., Guo, R.,  
551 Ke, P., Sun, T., Lu, C., He, P., Wang, Y., Yue, X., Wang, Y., Lei, Y., Zhou, H., Cai, Z., Wu, Y., Guo, R.,  
552 Han, T., Xue, J., Boucher, O., Boucher, E., Chevallier, F., Tanaka, K., Wei, Y., Zhong, H., Kang, C.,  
553 Zhang, N., Chen, B., Xi, F., Liu, M., Bréon, F.-M., Lu, Y., Zhang, Q., Guan, D., Gong, P., Kammen, D.  
554 M., He, K., and Schellnhuber, H. J.: Near-real-time monitoring of global CO<sub>2</sub> emissions reveals the  
555 effects of the COVID-19 pandemic, *Nature Communications*, 11, 5172,  
556 <https://doi.org/10.1038/s41467-020-18922-7>, 2020c.

557 MacDonald, C. G., Mastrogiacomo, J. P., Laughner, J. L., Hedelius, J. K., Nassar, R., and Wunch,  
558 D.: Estimating enhancement ratios of nitrogen dioxide, carbon monoxide and carbon dioxide  
559 using satellite observations, *Atmos. Chem. Phys.*, 23, 3493-3516, <https://doi.org/10.5194/acp-23-3493-2023>, 2023.

560  
561 Martin, R. V., Jacob, D. J., Chance, K., Kurosu, T. P., Palmer, P. I., and Evans, M. J.: Global  
562 inventory of nitrogen oxide emissions constrained by space-based observations of NO<sub>2</sub> columns,  
563 *Journal of Geophysical Research: Atmospheres*, 108, <https://doi.org/10.1029/2003JD003453>,  
564 2003.

565 Meinshausen, M., Lewis, J., McGlade, C., Gutschow, J., Nicholls, Z., Burdon, R., Cozzi, L., and  
566 Hackmann, B.: Realization of Paris Agreement pledges may limit warming just below 2 degrees  
567 C, *Nature*, 604, 304-309, <https://doi.org/10.1038/s41586-022-04553-z>, 2022.

568 Miyazaki, K. and Bowman, K.: Predictability of fossil fuel CO<sub>2</sub> from air quality emissions, *Nature*  
569 *Communications*, 14, 1604, <https://doi.org/10.1038/s41467-023-37264-8>, 2023.

570 Mun, J., Choi, Y., Jeon, W., Lee, H. W., Kim, C.-H., Park, S.-Y., Bak, J., Jung, J., Oh, I., Park, J., and  
571 Kim, D.: Assessing mass balance-based inverse modeling methods via a pseudo-observation test  
572 to constrain NO<sub>x</sub> emissions over South Korea, *Atmospheric Environment*, 292, 119429,  
573 <https://doi.org/10.1016/j.atmosenv.2022.119429>, 2023.

574 Nassar, R., Hill, T. G., McLinden, C. A., Wunch, D., Jones, D. B. A., and Crisp, D.: Quantifying CO<sub>2</sub>  
575 Emissions From Individual Power Plants From Space, *Geophysical Research Letters*, 44, 10,045-  
576 010,053, 10.1002/2017GL074702, 2017.

577 Reuter, M., Buchwitz, M., Schneising, O., Krautwurst, S., O'Dell, C. W., Richter, A., Bovensmann,  
578 H., and Burrows, J. P.: Towards monitoring localized CO<sub>2</sub> emissions from space: co-located  
579 regional CO<sub>2</sub> and NO<sub>2</sub> enhancements observed by the OCO-2 and S5P satellites, *Atmos. Chem.*  
580 *Phys.*, 19, 9371-9383, <https://doi.org/10.5194/acp-19-9371-2019>, 2019.

581 Roten, D., Lin, J. C., Das, S., and Kort, E. A.: Constraining Sector-Specific CO<sub>2</sub> Fluxes Using Space-  
582 Based XCO<sub>2</sub> Observations Over the Los Angeles Basin, *Geophysical Research Letters*, 50,  
583 e2023GL104376, <https://doi.org/10.1029/2023GL104376>, 2023.

584 Shan, Y., Ou, J., Wang, D., Zeng, Z., Zhang, S., Guan, D., and Hubacek, K.: Impacts of COVID-19  
585 and fiscal stimuli on global emissions and the Paris Agreement, *Nature Climate Change*, 11, 200-  
586 206, <https://doi.org/10.1038/s41558-020-00977-5>, 2021.

587 Sierk, B., Fernandez, V., Bézy, J.-L., Meijer, Y., Durand, Y., Bazalgette Courrèges-Lacoste, G.,  
588 Pachot, C., Löscher, A., Nett, H., Minoglou, K., Boucher, L., Windpassinger, R., Pasquet, A., Serre,  
589 D., and te Hennepe, F.: The Copernicus CO2M mission for monitoring anthropogenic carbon  
590 dioxide emissions from space, *International Conference on Space Optics — ICSO 2021, SPIE2021*.

591 Taylor, T. E., O'Dell, C. W., Baker, D., Bruegge, C., Chang, A., Chapsky, L., Chatterjee, A., Cheng,  
592 C., Chevallier, F., Crisp, D., Dang, L., Drouin, B., Eldering, A., Feng, L., Fisher, B., Fu, D., Gunson,  
593 M., Haemmerle, V., Keller, G. R., Kiel, M., Kuai, L., Kurosu, T., Lambert, A., Laughner, J., Lee, R.,  
594 Liu, J., Mandrake, L., Marchetti, Y., McGarragh, G., Merrelli, A., Nelson, R. R., Osterman, G.,  
595 Oyafuso, F., Palmer, P. I., Payne, V. H., Rosenberg, R., Somkuti, P., Spiers, G., To, C., Weir, B.,  
596 Wennberg, P. O., Yu, S., and Zong, J.: Evaluating the consistency between OCO-2 and OCO-3  
597 XCO<sub>2</sub> estimates derived from the NASA ACOS version 10 retrieval algorithm, *Atmos. Meas. Tech.*,  
598 16, 3173-3209, 10.5194/amt-16-3173-2023, 2023.

599 Turner, A. J., Henze, D. K., Martin, R. V., and Hakami, A.: The spatial extent of source influences  
600 on modeled column concentrations of short-lived species, *Geophysical Research Letters*, 39,  
601 <https://doi.org/10.1029/2012GL051832>, 2012.

602 van Geffen, J., Eskes, H., Compornolle, S., Pinardi, G., Verhoelst, T., Lambert, J. C., Sneep, M., ter  
603 Linden, M., Ludewig, A., Boersma, K. F., and Veefkind, J. P.: Sentinel-5P TROPOMI NO<sub>2</sub> retrieval:  
604 impact of version v2.2 improvements and comparisons with OMI and ground-based data,  
605 *Atmos. Meas. Tech.*, 15, 2037-2060, <https://doi.org/10.5194/amt-15-2037-2022>, 2022.

606 Wang, Z., Zhang, M., Li, H., Wang, L., Gong, W., and Ma, Y.: Bias correction and variability  
607 attribution analysis of surface solar radiation from MERRA-2 reanalysis, *Climate Dynamics*,  
608 10.1007/s00382-023-06873-w, 2023.

609 Wei, J., Liu, S., Li, Z., Liu, C., Qin, K., Liu, X., Pinker, R. T., Dickerson, R. R., Lin, J., Boersma, K. F.,  
610 Sun, L., Li, R., Xue, W., Cui, Y., Zhang, C., and Wang, J.: Ground-Level NO<sub>2</sub> Surveillance from Space  
611 Across China for High Resolution Using Interpretable Spatiotemporally Weighted Artificial  
612 Intelligence, *Environ Sci Technol*, 56, 9988-9998, 10.1021/acs.est.2c03834, 2022.

613 Wren, S. N., McLinden, C. A., Griffin, D., Li, S.-M., Cober, S. G., Darlington, A., Hayden, K., Mihele,  
614 C., Mittermeier, R. L., Wheeler, M. J., Wolde, M., and Liggio, J.: Aircraft and satellite  
615 observations reveal historical gap between top-down and bottom-up CO<sub>2</sub> emissions from  
616 Canadian oil sands, *PNAS Nexus*, 2, <https://doi.org/10.1093/pnasnexus/pgad140>, 2023.

617 Yang, E. G., Kort, E. A., Ott, L. E., Oda, T., and Lin, J. C.: Using Space-Based CO<sub>2</sub> and NO<sub>2</sub>  
618 Observations to Estimate Urban CO<sub>2</sub> Emissions, *Journal of Geophysical Research: Atmospheres*,  
619 128, e2022JD037736, <https://doi.org/10.1029/2022JD037736>, 2023.

620 Yang, E. G., Kort, E. A., Wu, D., Lin, J. C., Oda, T., Ye, X., and Lauvaux, T.: Using Space-Based  
621 Observations and Lagrangian Modeling to Evaluate Urban Carbon Dioxide Emissions in the  
622 Middle East, *Journal of Geophysical Research: Atmospheres*, 125, e2019JD031922,  
623 <https://doi.org/10.1029/2019JD031922>, 2020.

624 Ye, C., Zhou, X., Pu, D., Stutz, J., Festa, J., Spolaor, M., Tsai, C., Cantrell, C., Mauldin, R. L.,  
625 Campos, T., Weinheimer, A., Hornbrook, R. S., Apel, E. C., Guenther, A., Kaser, L., Yuan, B., Karl,  
626 T., Haggerty, J., Hall, S., Ullmann, K., Smith, J. N., Ortega, J., and Knote, C.: Rapid cycling of  
627 reactive nitrogen in the marine boundary layer, *Nature*, 532, 489-491, 10.1038/nature17195,  
628 2016.

629 Ye, X., Lauvaux, T., Kort, E. A., Oda, T., Feng, S., Lin, J. C., Yang, E. G., and Wu, D.: Constraining  
630 Fossil Fuel CO<sub>2</sub> Emissions From Urban Area Using OCO-2 Observations of Total Column CO<sub>2</sub>,  
631 *Journal of Geophysical Research: Atmospheres*, 125, e2019JD030528,  
632 <https://doi.org/10.1029/2019JD030528>, 2020.

633 Zhang, Q., Boersma, K. F., Zhao, B., Eskes, H., Chen, C., Zheng, H., and Zhang, X.: Quantifying  
634 daily NO<sub>x</sub> and CO<sub>2</sub> emissions from Wuhan using satellite observations from TROPOMI and OCO-  
635 2, *Atmos. Chem. Phys.*, 23, 551-563, 10.5194/acp-23-551-2023, 2023.

636 Zhang, Q., Zheng, Y., Tong, D., Shao, M., Wang, S., Zhang, Y., Xu, X., Wang, J., He, H., Liu, W.,  
637 Ding, Y., Lei, Y., Li, J., Wang, Z., Zhang, X., Wang, Y., Cheng, J., Liu, Y., Shi, Q., Yan, L., Geng, G.,  
638 Hong, C., Li, M., Liu, F., Zheng, B., Cao, J., Ding, A., Gao, J., Fu, Q., Huo, J., Liu, B., Liu, Z., Yang, F.,  
639 He, K., and Hao, J.: Drivers of improved PM<sub>2.5</sub> air quality in China from 2013 to 2017, *Proc Natl*  
640 *Acad Sci USA*, 116, 24463-24469, 10.1073/pnas.1907956116, 2019.

641 Zhao, Y., Nielsen, C. P., Lei, Y., McElroy, M. B., and Hao, J.: Quantifying the uncertainties of a  
642 bottom-up emission inventory of anthropogenic atmospheric pollutants in China, *Atmos. Chem.*  
643 *Phys.*, 11, 2295-2308, 10.5194/acp-11-2295-2011, 2011.

644 Zheng, B., Geng, G., Ciais, P., Davis, S. J., Martin, R. V., Meng, J., Wu, N., Chevallier, F., Broquet,  
645 G., Boersma, F., van der A, R., Lin, J., Guan, D., Lei, Y., He, K., and Zhang, Q.: Satellite-based  
646 estimates of decline and rebound in China's CO<sub>2</sub> emissions during COVID-19 pandemic, *Science*  
647 *Advances*, 6, eabd4998, <https://doi.org/10.1126/sciadv.abd4998>, 2020.

648 Zheng, B., Tong, D., Li, M., Liu, F., Hong, C., Geng, G., Li, H., Li, X., Peng, L., Qi, J., Yan, L., Zhang,  
649 Y., Zhao, H., Zheng, Y., He, K., and Zhang, Q.: Trends in China's anthropogenic emissions since  
650 2010 as the consequence of clean air actions, *Atmos. Chem. Phys.*, 18, 14095-14111,  
651 10.5194/acp-18-14095-2018, 2018.

652